

Dusty spirals versus gas kinematics in the inner kiloparsec of Four Low-Luminosity Active Galactic Nuclei

Carine Brum,^{1*} Rogemar A. Riffel¹, Thaisa Storchi-Bergmann²,
Andrew Robinson³, Allan Schnorr Müller² and Davide Lena^{4,5}

¹ Universidade Federal de Santa Maria, Departamento de Física, CCNE, 97105-900, Santa Maria, RS, Brazil

² Universidade Federal do Rio Grande do Sul, Instituto de Física, CP 15051, Porto Alegre 91501-970, RS, Brazil

³ Department of Physics, Rochester Institute of Technology, 84 Lomb Memorial Drive, Rochester, NY 14623, USA

⁴ SRON, Netherlands Institute for Space Research, Sorbonnelaan 2, NL-3584 CA Utrecht, the Netherlands.

⁵ Department of Astrophysics/IMAPP, Radboud University, Nijmegen, PO Box 9010, NL-6500 GL Nijmegen, the Netherlands.

7 November 2018

ABSTRACT

We used the Gemini Multi-Object Spectrograph (GMOS) Integral Field Unit (IFU) to map the gas distribution, excitation and kinematics within the inner kiloparsec of four nearby low-luminosity active galaxies: NGC3982, NGC4501, NGC2787 and NGC4450. The observations cover the spectral range 5600–7000 Å at a velocity resolution of 120 km s⁻¹ and spatial resolution ranging from 50 to 70 pc at the galaxies. Extended emission in H α , [N II] $\lambda\lambda$ 6548,6583, [S II] $\lambda\lambda$ 6716,6730 over most of the field-of-view is observed for all galaxies, while only NGC3982 shows [O I] λ 6300 extended emission. The H α equivalent widths ($W_{H\alpha}$) combined with the [N II]/H α line ratios reveal that NGC3982 and NGC4450 harbor Seyfert nuclei surrounded by regions with LINER excitation, while NGC2787 and NGC4501 harbor LINER nuclei. NGC3982 shows a partial ring of recent star-formation at 500 pc from the nucleus, while in NGC4501 a region at 500pc west of the nucleus shows LINER excitation but has been interpreted as an aging H II region with the gas excitation dominated by shocks from supernovae. The line-of-sight velocity field of the gas shows a rotation pattern for all galaxies, with deviations from pure disk rotation observed in NGC3982, NGC 4501 and NGC 4450. For NGC4501 and NGC4450, many of these deviations are spatially coincident with dust structures seen in optical continuum images, leading to the interpretation that the deviations are due to shocks in the gas traced by the dust. A speculation is that these shocks lead to loss of angular momentum, allowing the gas to be transferred inwards to feed the AGN. In the case of NGC2787, instead of deviations in the rotation field, we see a misalignment of 40° between the orientation of the line of nodes of the gas rotation and the photometric major axis of the galaxy. Evidence of compact nuclear outflows are seen in NGC4501 and NGC4450.

Key words: galaxies: individual (NGC 3982, NGC 4501, NGC 2787, NGC 4450) – galaxies: Seyfert – galaxies: kinematics and dynamics

1 INTRODUCTION

Understanding how mass is transferred from galactic scales down to nuclear scales to feed the super-massive black hole (SMBH) in the nuclei of galaxies has been the goal of many theoretical studies and simulations (Shlosman et al. 1990; Maciejewski 2002; Emsellem et al. 2003; Knapen 2005; Emsellem et al. 2006, 2015; Li, Shen & Kim. 2015; Capelo & Dotti 2017). These works have shown that non-axisymmetric potentials efficiently promote gas inflow toward the inner kiloparsec of galaxies (e.g. Englmaier &

Shlosman 2004), resulting in a gas reservoir that can trigger and maintain an Active Galactic Nucleus (AGN) and/or nuclear star formation.

Nuclear bars and associated spiral arms are indeed frequently observed in the inner kiloparsec of active galaxies (e.g. Erwin & Sparke 1999; Pogge & Martini 2002; Laine et al. 2003). Simões Lopes et al. (2007) found a strong correlation between the presence of the nuclear dusty structures (filaments, spirals, discs and bars) and nuclear activity in a sample of early-type galaxies, suggesting that a reservoir of gas and dust is a necessary condition for a galaxy to harbor an AGN. This correlation between the presence of dusty structures and nuclear activity supports the hypothesis that these structures represent a fueling mechanism for the SMBH, allowing

* E-mail: carinefisica@gmail.com

the gas to loose angular momentum and stream towards the center of the galaxies.

Previous studies by our group (e.g. Fathi et al. 2006; Storchi-Bergmann et al. 2007; Schnorr–Müller et al. 2011, 2014a,b), have revealed kinematic features associated with nuclear spirals, bars or filaments, that are consistent with gas inflow to the inner tens of parsecs of active galaxies. Motivated by these results, we have mapped the gaseous kinematics of four nearby AGNs showing dusty nuclear spirals, with the goal of looking for correlations between these spirals and the gas kinematics. The galaxies NGC 3982, NGC 4501, NGC 2787 and NGC 4450 were selected from the work by Simões Lopes et al. (2007), that was based mostly on low-luminosity AGNs. This study is part of a larger project in which we are obtaining optical integral field spectroscopic observations of a complete X-ray selected sample with the aim of investigating feeding and feedback mechanisms over a range in AGN luminosity (e.g. Schnorr–Müller et al. 2014a; Lena et al. 2015).

This work is organized as follows: Section 2 presents a description of the observations and data reduction procedure, Sec. 3 shows the emission-line flux distributions, line-ratio maps, velocity fields and velocity dispersion maps. In Sec. 4 we model the velocity fields and in Sec. 5 we discuss the results for each galaxy. Finally, in Sec. 6, we present the main conclusions of this work.

2 OBSERVATIONS AND DATA REDUCTION

As pointed out above, the four active galaxies of this study were selected from the sample of Simões Lopes et al. (2007) by showing dusty nuclear spirals in Hubble Space Telescope (HST) optical images through the filter F606W, and revealed in “structure maps” that are aimed to enhance fine structural features in single-filter images (Pogge & Martini 2002). The observations were obtained using the Gemini Multi-Object Spectrograph Integral Field Unit (GMOS-IFU, Allington-Smith et al. 2002; Hook et al. 2004) at the Gemini North Telescope in 2007, 2008 and 2011.

We have observed the wavelength range 5600–7000 Å, which includes the strongest emission lines, as H α , [N II] $\lambda\lambda$ 6548, 6583, [S II] $\lambda\lambda$ 6716, 6730 and [O I] λ 6300, using the IFU in the two slit mode. The R400 grating was used in combination with the r (530 nm) filter, resulting in a spectral resolution of 2.5–2.7 Å, as obtained from the full-width at half maximum (FWHM) of arc lamp lines used to wavelength calibrate the spectra, translating to \sim 100–125 km s $^{-1}$ in velocity space.

The data comprise three adjacent IFU fields for NGC 3982, NGC 4501 and NGC 4450, each one covering 5" \times 7", while for NGC 2787 we used two adjacent IFU fields. In order to remove cosmic rays and bad pixels small spatial offsets were performed between individual exposures at each position. The final Field of View (FoV), obtained after mosaicking the individual cubes for each galaxy are approximately 7" \times 15" for NGC 3982 and NGC 4501, 7" \times 9" for NGC 2787 and 20" \times 5" for NGC 4450, with the longest dimension of the FoV oriented along the major axis of each galaxy. The total exposure time for each galaxy ranges from 75 to 82 minutes. Table 1 shows the log of the observations, as well as relevant information on each galaxy.

Data reduction was performed using the IRAF¹ packages provided by the Gemini Observatory and specifically developed for the

GMOS instrument. First, the bias was subtracted from each image, followed by flat-fielding and trimming of the spectra. The wavelength calibration was applied to the science data using as reference the spectra of Arc lamps, followed by subtraction of the underlying sky emission. To obtain a relative flux calibration we constructed a sensitivity function using the spectra of standard stars provided by the observatory as default calibrations. Feige 66 was used as standard star for NGC 4501, while Feige 34 was used for NGC 2787 and BD+28d4211 was used for NGC 3982 and NGC 4450. Finally, separate data cubes were obtained for each exposure, which were then aligned and median combined to a single cube for each galaxy. All individual cubes were created with 0'.05 square spaxels during the data reduction, but for NGC 4450 the final data cube was rebinned to 0'.15 square spaxels in order to increase the signal to noise ratio of the spectra and allow the fitting of the emission-lines profiles at locations away from the nucleus.

The spatial resolution of the final data cubes, presented in Table 1, are in the range 50–70 pc and were obtained from average FWHM of the flux distribution of field stars seen in the acquisition image at the r band, and adopting the distances quoted in the forth column of the same table. The uncertainty in the spatial resolution is about 10% for all galaxies, estimated as the standard deviation of the average FWHM.

3 RESULTS

Figure 1 shows a large scale image and typical spectra for each galaxy. At the top-right corner of each image, we show as an insert the structure map of the inner 20" \times 20". The orientation is shown by the arrows in the top-left corner of each image. The central box at the HST structure map shows the IFU FoV. These structure maps were constructed following Simões Lopes et al. (2007) using HST broad band images obtained through the F606W filter (from Malkan, Gorjian & Tam 1998) and are aimed to highlight dust structures present in the inner region of the galaxies. The structure maps reveal dust structures for all galaxies: NGC 3982 clearly shows dust spiral structures from 10" down to the nucleus; NGC 4501 shows much more dust to the northeast than to the southwest; NGC 2787 shows elliptical dusty partial rings that seem to be concentric and NGC 4450 presents a complex dust distribution with more dust to the east of the nucleus, and a dusty blob to the northwest.

The right panels of Fig 1 show two spectra for each galaxy obtained within a circular aperture of 0'.25 radius (corresponding to 5 pixels) for NGC 3982, NGC 4501 and NGC 2787, and 0'.45 radius (corresponding to 3 pixels) for NGC 4450. The first spectrum correspond to the nucleus and the other were obtained for the position labeled as “A” in the flux distributions maps of Figures 2–5, chosen to represent typical extra-nuclear spectra. The strongest emission lines are identified.

3.1 Measurements

In order to measure the emission-line flux distributions and gas kinematics, we fitted the line profiles of H α + [N II] $\lambda\lambda$ 6548, 6584, [S II] $\lambda\lambda$ 6717, 6731 and [O I] λ 6300 by single Gaussian curves using a modified version of the PROFIT routine (Riffel et al. 2010). This routine performs the fit of the observed profile using the MPFIT-FUN routine (Markwardt et al. 2009), via a non-linear least-squares fit. In order to reduce the number of free parameters, we adopted

¹ IRAF is distributed by National Optical Astronomy Observatories, which are operated by the Association of Universities for Research in Astronomy, Inc., under cooperative agreement with the National Science Foundation

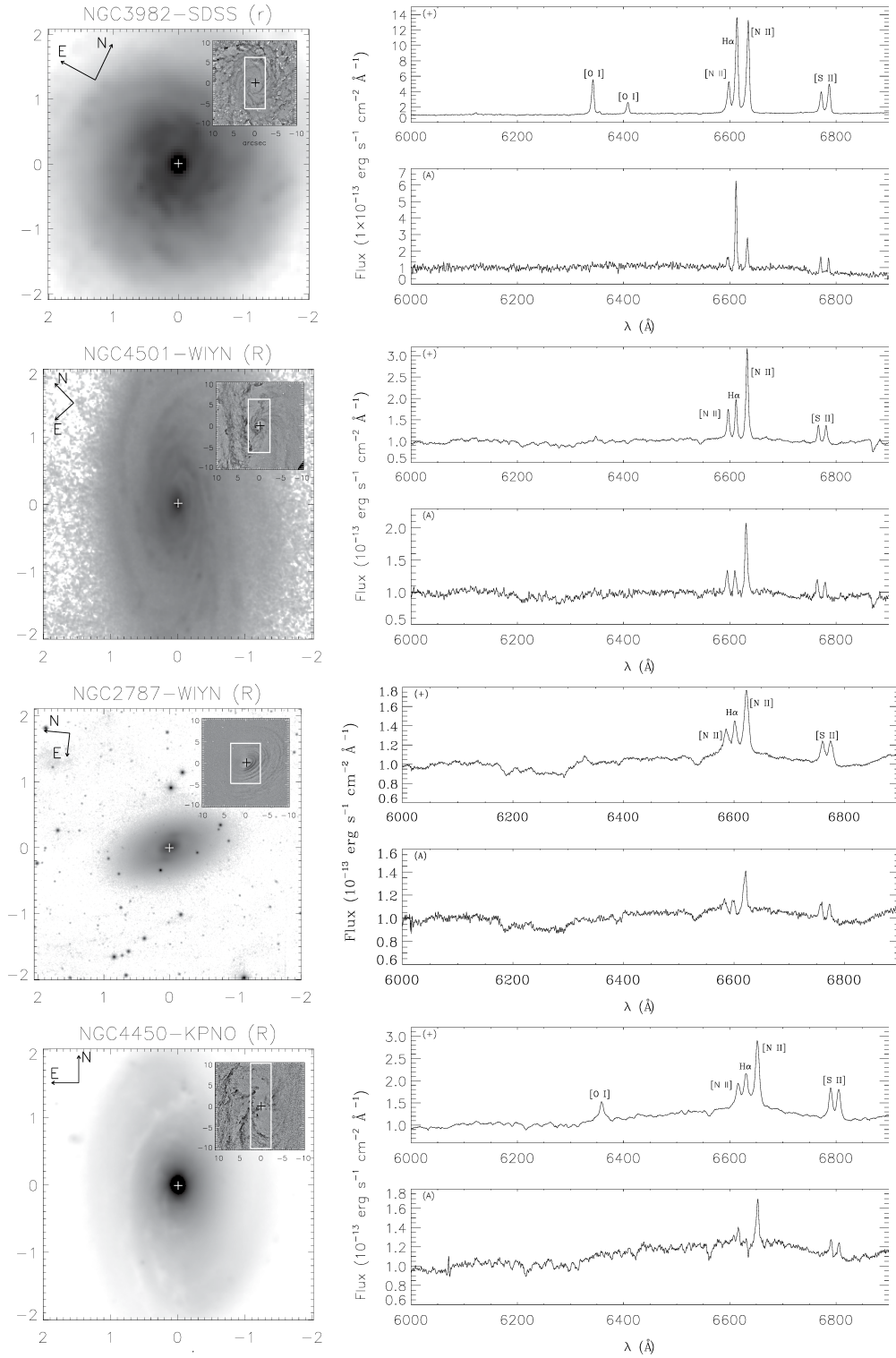


Figure 1. Left panels: large-scale image obtained from SDSS (Baillard et al. 2011) for NGC 3982, from Koopmann, Kenney & Young (2001) for NGC 4501 and NGC 2787 and from Young et al. (1996) for NGC 4450. Insert in the top right corner of in each left panel: structure map obtained from an HST-WFPC2 F606W image (Simões Lopes et al. 2007) of the inner 20'' × 20''. Right panels show spectra from the nucleus (labeled as '+'), and positions "A" identified at the flux distribution image of in Figs. 3 and A2. These spectra were extracted within a circular aperture of 0''.25 radius.

Table 1. Observing log and properties of the sample

Galaxy	Nuc. act.	Hubble Type	d (Mpc)	Obs. Date	Exp. Time ¹	NFoV	FoV	Spec. Res.	Spat. Res.	Gemini Project
NGC 3982	Seyfert 2	SAB(r)b ²	17.0 ²	01/01/2007	3×520	3	7′1×15′3	2.7Å	70 pc (0′85)	GN-2006B-Q-94
NGC 4501	Seyfert 2	SA(rs)b ³	16.8 ²	02/14/2008	3×500	3	7′3×15′5	2.5Å	60 pc (0′75)	GN-2008A-Q-8
NGC 2787	LINER	SB(r)0 ⁺ 2	13.0 ²	01/27/2011	4×615	2	7′0×9′2	2.5Å	50 pc (0′80)	GN-2011A-Q-85
NGC 4450	LINER	SAab ²	16.8 ²	01/03/2007	3×520	3	20′1×5′5	2.7Å	65 pc (0′80)	GN-2006B-Q-94

(1) Exposure time per FoV; (2) Ho et al. (1997). (3) de Vaucouleurs et al. (1991).

the following constraints: the [N II]+H α emission lines were fitted by keeping tied the kinematics of the [N II] lines and fixing the [N II] λ 6563/[N II] λ 6548 intensity ratio to its theoretical value (3). The [S II] doublet was fitted by keeping the kinematics of the two lines tied, while the [O I] λ 6300 was fitted individually with all parameters free. For the H α line all parameters were allowed to vary independently. In all cases, the continuum emission was fitted by a linear equation, as the spectral range of each line fit was small.

NGC 4450 presents a known broad double-peaked H α line (Ho et al. 2000), seen also in the nuclear spectrum of our GMOS data (Fig. 1). To take this broad double-peaked emission into account during the fit, we have included two additional broad components at locations closer to the nucleus than 1′′. As the Broad Line Region is not resolved, the width and central wavelength of each broad component were kept fixed to the values obtained by fitting the nuclear spectrum shown in Fig. 1, while the amplitude of each Gaussian was allowed to vary during the fit.

The fitting routine outputs a data cube with the emission-line fluxes, gas velocity, and velocity dispersion, as well as their corresponding uncertainties and χ^2 map. These cubes were used to construct two dimensional maps for these physical properties, presented in Figures 2 - 5, for NGC 3982, NGC 4501, NGC 2787 and NGC 4450, respectively, together with the HST structure map, an excitation diagram, excitation map and electronic density.

3.2 WHAN diagram and excitation map

In order to map the gas excitation, line-ratio diagnostic diagrams are frequently used, the most popular of them being the BPT diagrams (Baldwin, Phillips & Terlevich 1981). Integral field spectroscopy allows the construction of two-dimensional diagnostic diagrams (Sarzi et al. 2010; Sanchez et al. 2015; Colina et al. 2015; Belfiore et al. 2016). As our observations do not cover the [O III] λ 5007 and H β lines, we use an alternative diagnostic diagram recently proposed by Cid Fernandes et al. (2010), that makes use only of the H α and [N II] λ 65863 emission lines. This diagram plots the H α equivalent width against the [N II]/H α line ratio, and is usually referred to as the WHAN diagram (Cid Fernandes et al. 2010). The WHAN diagram allows the separation of Starbursts, Seyfert galaxies (or strong AGN: sAGN), weak AGN (wAGN, defined as having H α equivalent widths W (H α) between 3Å and 6Å), and retired galaxies (RGs), that is galaxies having W (H α) smaller than 3Å, not active, but displaying weak emission lines produced by radiation from post-AGB stars. A particular advantage of the WHAN diagram is to allow the separation between wAGN and RG, that overlap in the LINER region of traditional BPT diagnostic diagrams.

The spatially resolved WHAN diagnostic diagrams for each galaxy are shown in the top-central panels of Figures 2–5 and the top-right panels show the resulting excitation maps: distinct regions of the FoV color-coded according to the excitation derived from the WHAN diagram. White regions in the excitation maps correspond

to locations where we could not fit one or both emission lines. The color bar shows the identification of the distinct excitation classes.

The excitation map for NGC 3982 shows sAGN values within the inner 1′′ (82 pc), while SF excitation regime is observed in a ring at 4–6′′ from the nucleus and a mixture of RG, sAGN and wAGN is observed in between these regions. The excitation map of NGC 4501 and NGC 2787 show unresolved regions of wAGN excitation at their nuclei, surrounded by RG excitation regions. A similar behavior is observed for NGC 4450, but showing sAGN values at the nucleus. In addition, NGC 4501 presents sAGN values within an unresolved region at \sim 6′′ west of the nucleus (close to the border of the FoV).

3.3 Flux distributions

The flux distributions in the [N II] λ 6583 emission line for each galaxy is shown in the middle-left panels of Figures 2–5. Black regions represent masked locations where the uncertainty in the flux is larger than 30%, and we were not able to get good fits of the line profiles due to the low S/N ratio or non-detection of the corresponding emission line. Similar maps for the H α , [S II] and [O I] emission lines are shown in appendix A (Figures A1–A4). The [O I] λ 6300 Å flux maps show extended emission only for NGC 3982 and we thus do not show the corresponding flux maps for the other galaxies.

All galaxies present the gas emission peak at the nucleus for all emission lines.

The NGC 3982 flux maps for H α and [N II] show extended emission over the whole GMOS-IFU FoV (up to 574 pc (7′′) from the nucleus), with a partial ring of enhanced gas emission surrounding the nucleus at 328 - 492 pc (4 - 6′′) from it, attributed to star forming regions. The [S II] flux distribution also shows emission associated to the ring, but most of the [S II] emission is concentrated within $r = 164 - 328$ pc (2–4′′) from the nucleus. The [O I] emission is observed only within $r = 123$ pc (1.5′′) from the nucleus.

NGC 4501 presents extended emission for H α and [N II] up to 486 pc (6′′) from the nucleus. The [S II] flux map is more concentrated, with emission seen only within the inner 162 - 243 pc (2–3′′). All maps show the most extended emission along the northwest-southeast direction, approximately along the major axis of the galaxy as seen in Fig. 1. In addition, the H α map presents a small region with enhanced emission at \sim 486 pc (6′′) south-west of the nucleus attributed to an H II region.

Extended [N II] and [S II] emission over the whole FoV - up to 315 pc (5′′) from the nucleus is observed for NGC 2787, while the H α emission is more concentrated within the inner 126 - 189 pc (2 - 3′′).

For NGC 4450, the highest intensity levels show flux distributions slightly more elongated along the east-west direction, approximately perpendicular to the orientation of the major axis of the galaxy. At locations beyond 162 - 243 pc (2–3′′) from the nucleus, the [N II] and H α emission show two spiral arms, one to the

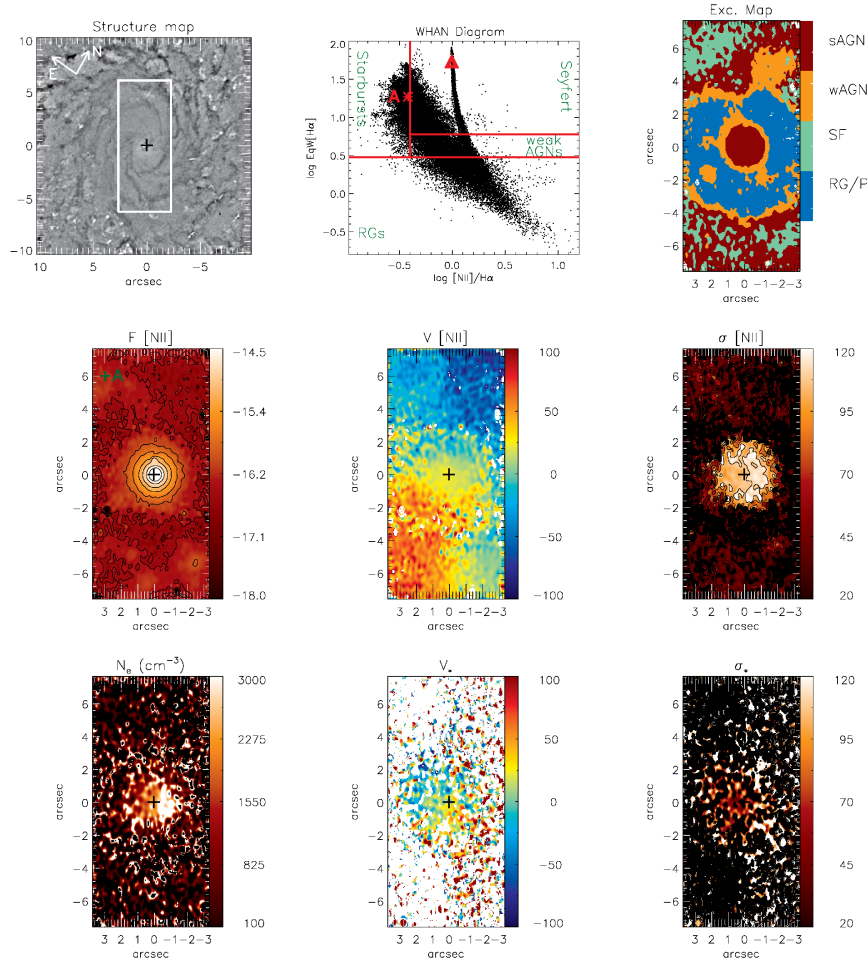


Figure 2. NGC 3982 - Top panels: structure map of the HST F606W image of the inner $20'' \times 20''$; the WHAN diagram showing the region occupied by the distinct excitation classes, where the $H\alpha$ equivalent width is shown in \AA ; the red triangle corresponds to the nucleus and the asterisks represents position A (see spectra in Fig. 1). Middle panels: flux distribution in logarithmic units of $\text{erg s}^{-1} \text{cm}^{-2}$; line-of-sight velocity field; and velocity dispersion map for the $[\text{N II}] \lambda 6583$ emission line, both in units of km s^{-1} . Bottom panels: gas density (cm^{-3}) derived from the $[\text{S II}]$ line ratio, stellar centroid velocity field (km s^{-1}) and stellar velocity dispersion (km s^{-1}). The central crosses mark the location of the nucleus.

north and another to the south of the nucleus, extending to up to 810 pc ($10''$) from it.

3.4 Velocity fields

The $[\text{N II}]$ velocity field for each galaxy is presented in the mid-central panels of Figures 2–5, with white regions corresponding to masked locations due to bad fits. Similar maps for the $H\alpha$, $[\text{S II}]$ and $[\text{O I}]$ emission lines are shown in Figures A1–A4.

The $H\alpha$ and $[\text{N II}]$ velocity fields for NGC 3982 present a rotation pattern with blueshifts observed to the north (thus this side is approaching) and redshifts to the south (and this side is receding), with a projected velocity amplitude of $\approx 100 \text{ km s}^{-1}$.

NGC 4501 also presents velocity fields consistent with gas rotating in the plane of the galaxy with blueshifts to the west and redshifts to the east, also showing deviations from pure rotation indicating the presence of non-circular motions at some locations. The velocity fields for all lines are similar, with deviations from rotation including excess redshifts at $\sim 162 \text{ pc}$ ($2''$) southwest of the nucleus, along the minor axis of the galaxy (where the velocities reach values of up to 150 km s^{-1}) and excess redshifts in a region

marginally resolved at $\sim 486 \text{ pc}$ ($6''$) west of the nucleus. The origin of these structures will be further discussed in Sec. 5.5.

The velocity fields for NGC 2787 are consistent with pure rotation in a disk oriented along position angle $PA \sim 50/230^\circ$ east of north, with blueshifts to the southwest and redshifts to the northeast and a high projected velocity amplitude of $\sim 250 \text{ km s}^{-1}$.

NGC 4450 also presents velocity fields indicating rotation in the disk of the galaxy, with blueshifts to the south and redshifts to the north of the nucleus, with a projected velocity amplitude of $\sim 150 \text{ km s}^{-1}$. In addition to the rotation pattern, excess blueshifts of up to -150 km s^{-1} are observed at $1''$ east of the nucleus, in a region comparable in size to the spatial resolution of our data.

3.5 Velocity dispersion maps

The $[\text{N II}]$ velocity dispersion map for each galaxy is presented in the mid-right panel of Figures 2–5, with black regions corresponding to masked locations due to bad fits. Similar maps for the $H\alpha$, $[\text{S II}]$ and $[\text{O I}]$ emission lines are shown in Figures A1–A4.

NGC 3982 shows σ values ranging from $\sim 50 \text{ km s}^{-1}$ to $\sim 130 \text{ km s}^{-1}$, with the highest values observed within 82 pc from the

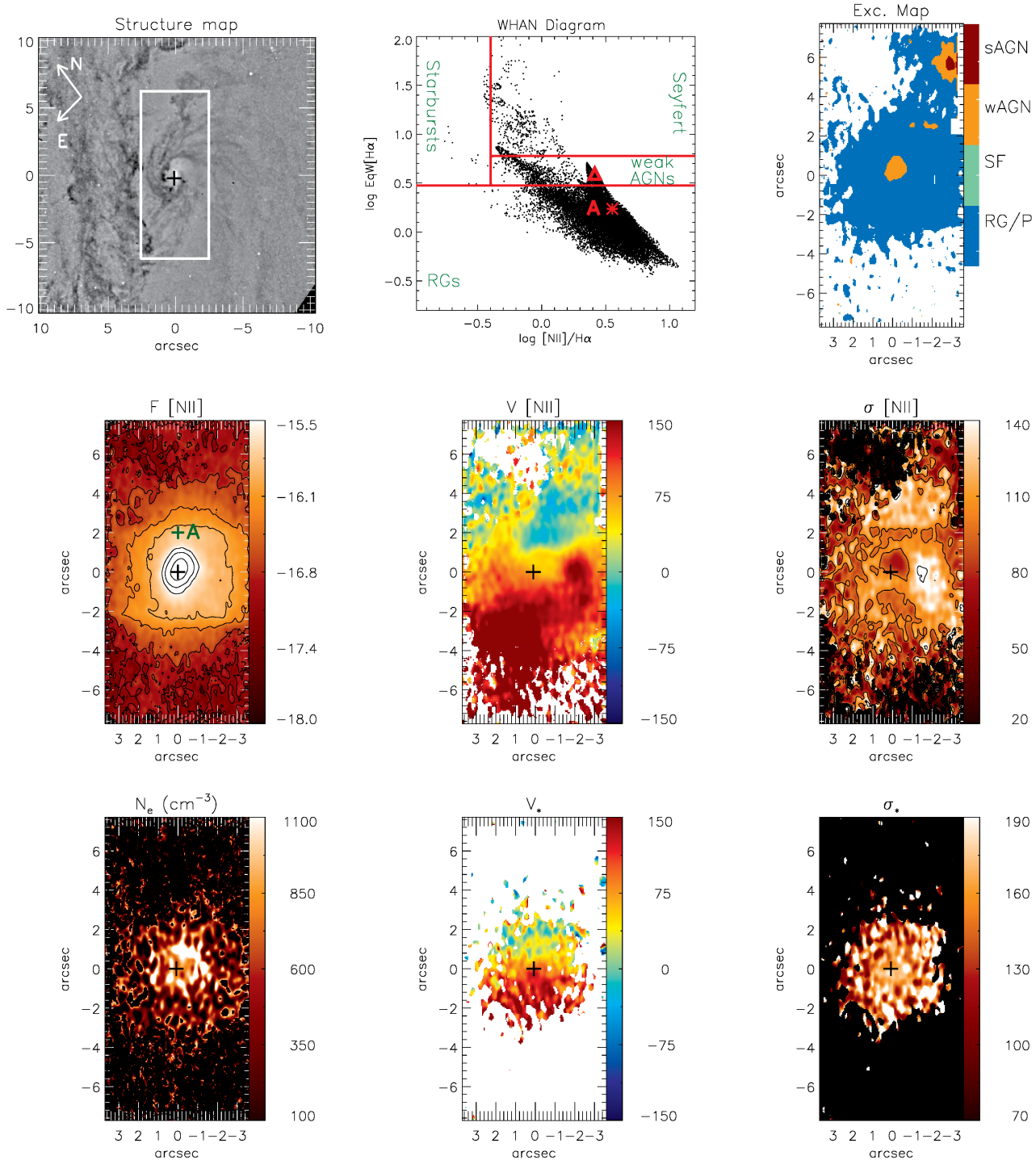


Figure 3. Same as Fig. 2 for NGC 4501.

nucleus and the smallest values in the partial circumnuclear star forming ring at 328 - 492 pc ($r \approx 4-6''$) from the nucleus. It can also be noticed that the forbidden lines show slightly larger σ values than $\text{H}\alpha$, suggesting that they trace emission from kinetically “hotter” gas.

The σ values for NGC 4501 are higher than $\sim 120 \text{ km s}^{-1}$ over a large part of the FoV, up to distances of 324 pc ($4''$) from the nucleus. Higher values of $\sim 150 \text{ km s}^{-1}$ are observed in a small patch

(89.1 pc \times 153.9 pc) at 121.5 pc ($1'5$) south of the nucleus. This region is co-spatial with excess redshifts observed in the velocity fields. On the other hand, very small σ values ($\sim 30-50 \text{ km s}^{-1}$) are observed at 486 pc ($6''$) west of the nucleus, where another region of excess redshifts is observed in Figs. 3 and A2. As for NGC 3982, the forbidden lines show an average σ value larger than those of $\text{H}\alpha$.

NGC 2787 shows the highest σ values of up to 150 km s^{-1}

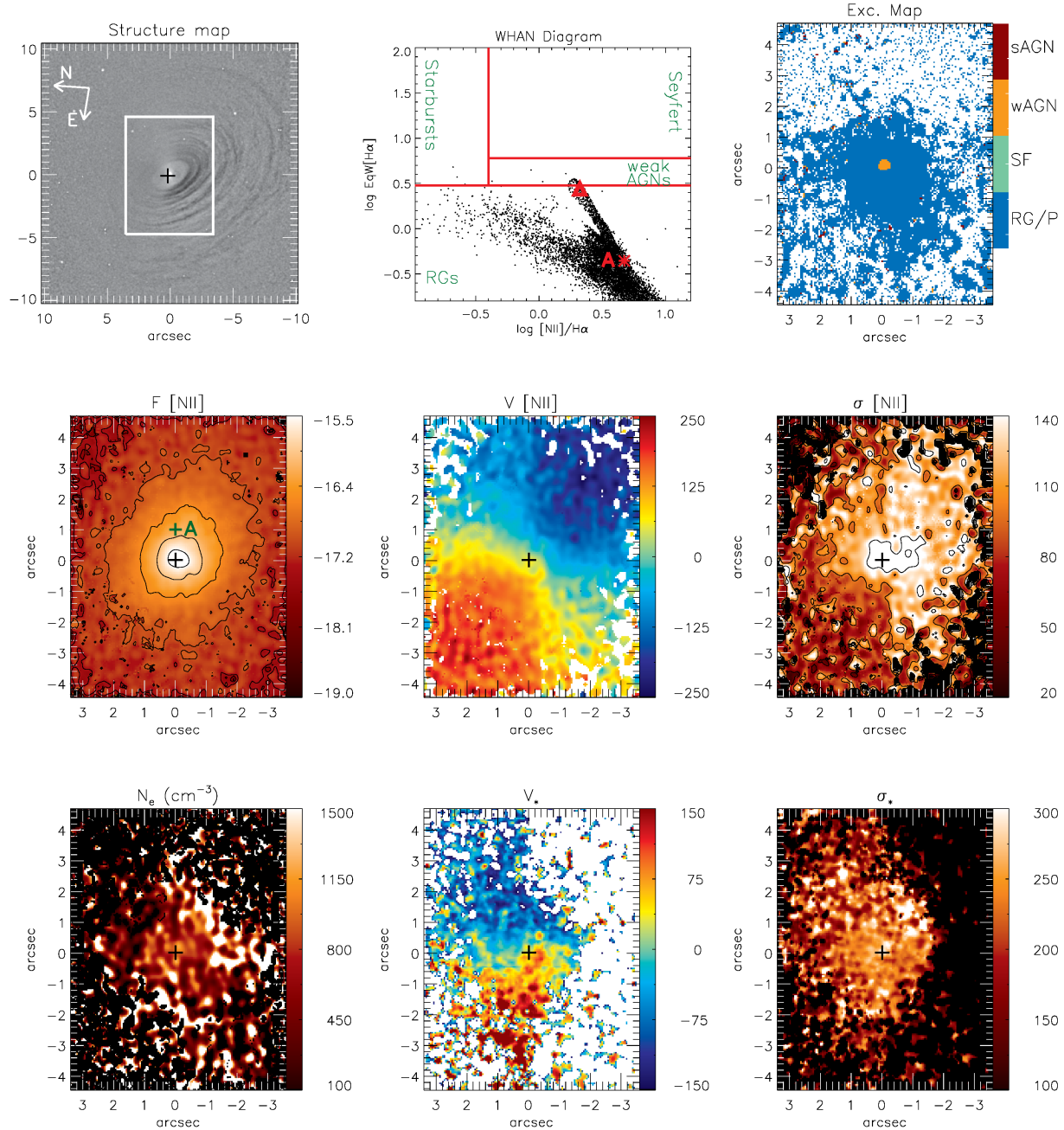


Figure 4. Same as Fig. 2 for NGC 2787.

within 63 pc from the nucleus for all emission lines. Outside the nucleus there is an asymmetry in the distribution of σ values: while to the south of the nucleus the lowest values of $\sim 30 - 60 \text{ km s}^{-1}$ are observed, to the northeast of the nucleus $\sigma \geq 120 \text{ km s}^{-1}$.

For NGC 4450 the highest σ values for all emission lines are observed within 81 pc from the nucleus. The $\text{H}\alpha$ and $[\text{S II}]$ show $\sigma \sim 100 \text{ km s}^{-1}$, while some higher values ($\sim 200 \text{ km s}^{-1}$) are observed for the $[\text{N II}]$ at these locations. The smallest σ values are $\sim 50 - 70 \text{ km s}^{-1}$, observed in the spiral arms.

3.6 Electron density

The ratio of the fluxes $[\text{S II}] \lambda 6716 / \lambda 6731$ was used to obtain the electron density N_e using the TEMDEN routine of the NEBULAR package from STSDAS/IRAF, assuming an electron temperature for the ionized gas of 10 000 K. The bottom left panels of Figures 2 - 5 show the gas electron density distribution for all galaxies.

The highest electron density values of about 3000 cm^{-3} are found within the inner 82 pc ($1''$) of NGC 3982. For the other galaxies the density values range from 600 to 1500 cm^{-3} , and are similar to those obtained in similar studies of the inner kiloparsec of active galaxies (e.g. Couto et al. 2013; Lena et al. 2015)

3.7 Stellar kinematics

In order to obtain measurements for the Line-of-Sight Velocity Distribution (LOSVD) of the stars we used the Penalized Pixel Fitting (pPXF) routine of Cappellari & Emsellem (2004) to fit stellar absorptions in the spectral range from 5600 – 6900 Å. The fitting of the galaxy spectra is done by using template spectra under the assumption that the LOSVD of the stars is well reproduced by Gauss-Hermite series. We used selected simple stellar population synthetic spectra from the Bruzual & Charlot (2003) models, which have similar spectral resolution to those of our GMOS data (e.g. Schnorr-Müller et al. 2014a).

The corresponding stellar velocity field and velocity dispersion (σ_*) maps for each galaxy are shown in the bottom-central and bottom-right panels of Figures 2–5. White/black regions in the velocity/velocity dispersion maps correspond to masked locations where the uncertainties of the measurements are larger than 50 km s⁻¹.

The stellar velocity fields of all galaxies show signatures of rotation. For NGC 3982, the stellar kinematic maps are very noisy, but the stellar velocity field shows a similar trend of rotating disk as observed for the gas, with blueshifts observed to the northeast of the nucleus and redshifts to southwest of it. We were able to measure the stellar kinematics only within the inner 2'' of NGC 4501, which shows a clear rotation pattern with blueshifts observed to the northwest of the nucleus and redshifts to southeast of it, with a velocity amplitude of ~150 km s⁻¹. A similar velocity amplitude is observed for NGC 2787 with blueshifts observed to the west and redshifts to the east, showing a similar signature of rotation as observed in the gas velocity field. The orientation of the line of nodes of the gas and stars seems to be misaligned by 30–40°. However, we were not able to fit the stellar absorptions at most locations to the south of the nucleus of this galaxy, possible due to the larger extinction at this side, as seen in the structure map (top-left panel of Figure 4). NGC 4450 shows a clear rotating disk pattern with the line of nodes oriented along the north-south direction. The deviations from pure rotation seen in the gas velocity field are not observed in the stellar velocity field of this galaxy.

The stellar velocity dispersion map of NGC 3982 shows values smaller than 100 km s⁻¹ at most locations, being smaller than that observed for the gas at the same locations. NGC 4501 shows σ_* values overall larger than those observed for the [N II] emitting gas and a partial low- σ_* ring ($\sigma_* < 100$ km s⁻¹) is observed surrounding the nucleus at 1''. Similar structures have been observed for other active galaxies and attributed to being originated from intermediate age (100 Myr – 2 Gyr) stellar populations (Riffel et al. 2010, 2011, 2017). For NGC 2787, the σ_* map shows values larger than 150 km s⁻¹ at most locations, suggesting that although the stellar velocity field shows a clear rotation pattern, the stellar motions are dominated by random orbits, instead of ordered rotation in the plane of the disk. Finally, NGC 4450 shows σ_* values in the range from 70 to 130 km s⁻¹, similar to that observed at extra-nuclear regions for the gas.

4 ROTATION DISK MODEL

As seen in Figs. 2–5, both the gas and the stellar velocity fields for all galaxies show a rotation pattern, with the gas presenting some deviations from pure rotation due to non-circular motions. Here we model only the gas velocity fields with a rotation model due to the fact that the stellar velocity fields are much noisier but present similar rotation patterns. We used a simple analytical model, assuming

that the gas has circular orbits at the plane of the galaxy (van der Kruit & Allen 1978; Bertola et al. 1991), as done in previous works by our group (e.g. Couto et al. 2013; Schnorr-Müller et al. 2014a,b; Lena et al. 2015, 2016). The expression for the circular velocity is given by

$$V_{\text{mod}}(R, \Psi) = v_s + \frac{AR \cos(\Psi - \Psi_0) \sin(i) \cos^p(i)}{\left\{R^2[\sin^2(\Psi - \Psi_0) + \cos^2(i) \cos^2(\Psi - \Psi_0)] + C_o^2 \cos^2(i)\right\}^{p/2}}, \quad (1)$$

where A is the velocity amplitude, Ψ_0 is the position angle of the line of nodes, C_o is a concentration parameter, defined as is the radius where the rotation curve reaches 70 % of the velocity amplitude, i is the disc inclination in relation to the plane of the sky ($i = 0$ for face-on disc), R is the radial distance to the nucleus projected in the plane of the sky with the corresponding position angle Ψ , and v_s is the systemic velocity of the galaxy. The parameter p measures the slope of the rotation curve where it flattens, in the outer region of the galaxy and it is limited between $1 \leq p \leq 3/2$. For $p = 1$ the rotation curve at large radii is asymptotically flat while for $p = 3/2$ the system has a finite mass.

We used an IDL² based routine to fit the above equation to the observed [N II]λ6583 velocity fields using the MPFITFUN routine (Markwardt et al. 2009) to perform the non-linear least-squares fit, where initial guesses are given for each parameter and the routine returns their values for the best fitted model. As all lines show similar velocity fields, we have chosen the [N II] kinematics to perform the fit, as the [N II]λ6583 is the strongest line observed at most locations for all galaxies. During the fit, the location of the kinematical center was fixed to the position of the peak of the continuum emission and the parameter p was fixed to $p = 1.5$.

In Figures 6–9 we show the [N II] velocity field (left panel), resulting model (middle left panel), the residual map (middle right panel) and a structure map (right panel) for NGC 3982, NGC 4501, NGC 2787 and NGC 4450, respectively, while the resulting fitted parameters are shown in table 2. The values of the disk inclination and the amplitude of the rotation curve are coupled, meaning that somewhat higher or lower inclinations give similar fits for corresponding somewhat smaller and larger amplitudes, respectively. A similar coupling is observed between i and c_0 and these values should thus be considered with caution.

5 DISCUSSION

In this section we present a small review of what is already known for each galaxy of our sample and discuss our results in comparison (or addition) to those of these previous works.

5.1 NGC3982

NGC 3982 (or UGC 6918) is part of the Ursa Major cluster. Optical and near-infrared broad band images reveal the presence of a small nuclear bar extending by 10'' along $PA \sim 30^\circ$ east of north, while at larger scales it displays a multi-armed spiral pattern, seen in a B-I color index map and H α narrow band images (Knapen et al. 2002; Regan, et al. 1999; Pérez-Ramírez et al. 2000). Multi-spiral arms are also seen at small scales, as revealed by the HST F606W image

² <http://www.harrisgeospatial.com/ProductsandSolutions/GeospatialProducts/IDL.aspx>

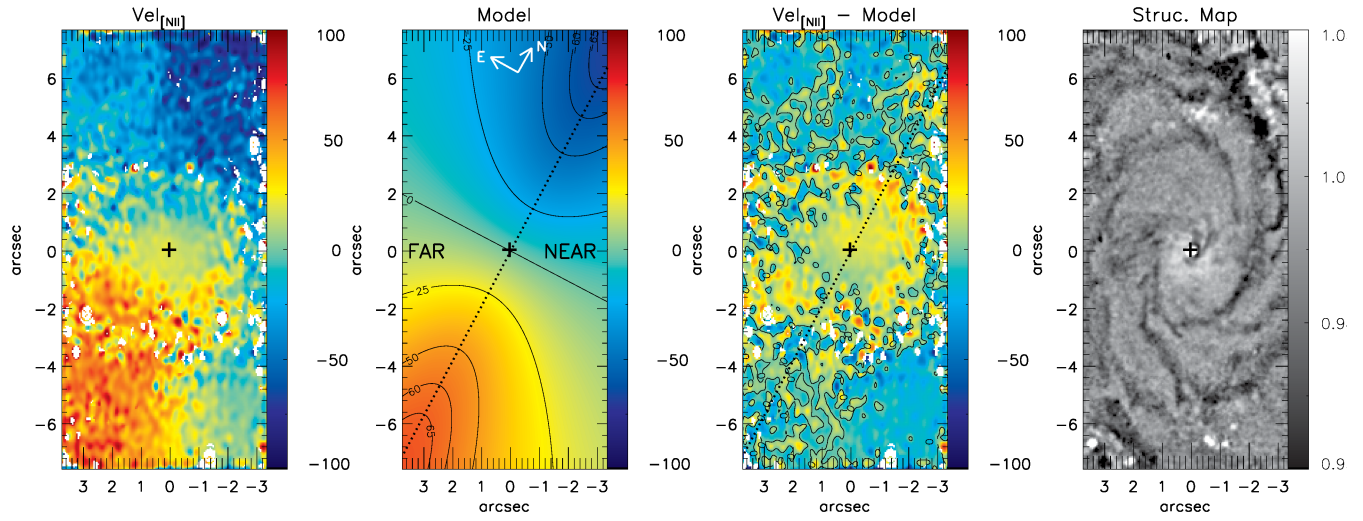


Figure 6. NGC 3982: From left to right: [N II] velocity field, rotating disc model for the [N II] velocity field (km s^{-1}), residual map (between the observed, modeled velocities) and structure map. The dotted line displays the position of the line of nodes, the structure map and the near and far sides of the galaxy are indicated.

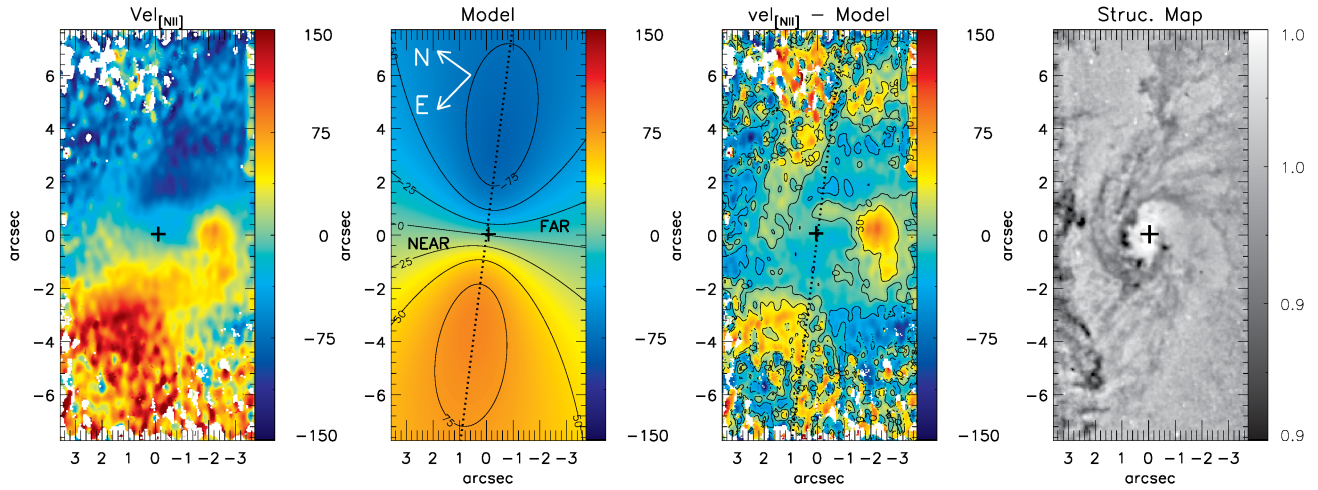


Figure 7. Same as Fig. 6 for NGC 4501

Table 2. Parameters derived from our modeling for galaxies

Galaxy	A (km s^{-1})	v_s (km s^{-1})	Ψ_0	c_o	i
NGC 3982	301 ± 5	1103 ± 10	$173^\circ \pm 2^\circ$	$6.8 \pm 0.1''$	$72^\circ \pm 2^\circ$
NGC 4501	206 ± 11	2244 ± 12	$133^\circ \pm 3^\circ$	$2.0 \pm 0.1''$	$47^\circ \pm 3^\circ$
NGC 2787	585 ± 4	615 ± 11	$76^\circ \pm 1^\circ$	$2.1 \pm 0.1''$	$46^\circ \pm 2^\circ$
NGC 4450	502 ± 13	1910 ± 10	$192^\circ \pm 4^\circ$	$6.5 \pm 0.3''$	$63^\circ \pm 3^\circ$

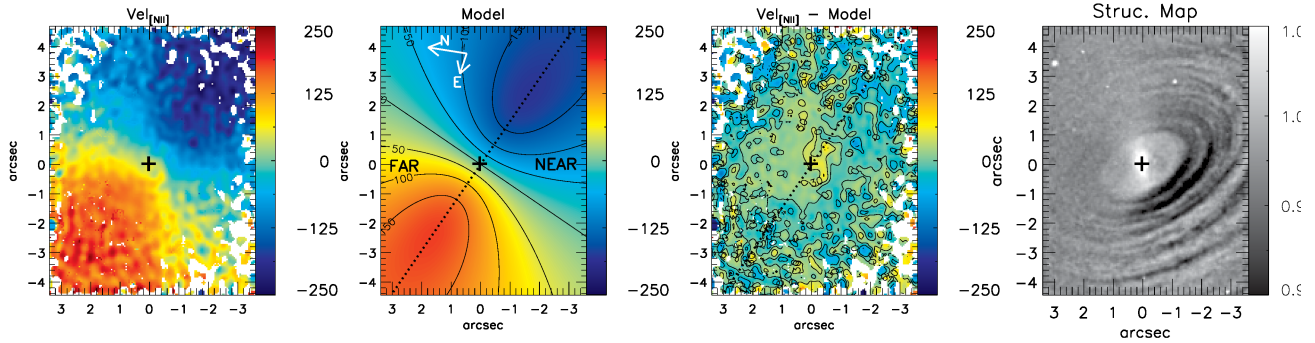


Figure 8. Same as Fig. 6 for NGC 2787

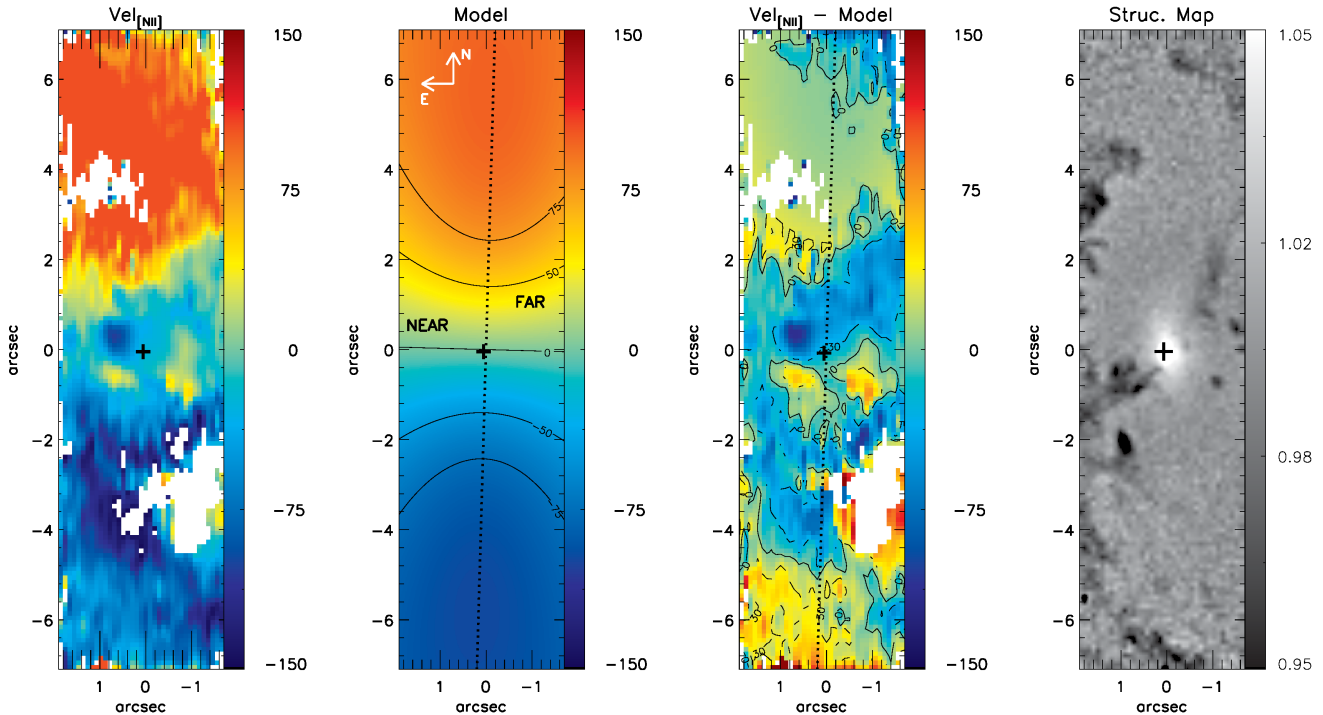


Figure 9. Same as Fig. 6 for NGC 4450

(Simões Lopes et al. 2007; Muñoz Marin et al. 2007). At radio wavelengths, a weak elongated feature of 4 kpc length is observed along the north-south direction in 6 cm, plus unresolved nuclear emission, probably due to the AGN (Ho & Ulvestad 2001). The radiation field of the AGN seems also to heat the dust close to the nucleus, as revealed by a very red near-IR color (Pérez-Ramírez et al. 2000). In addition, the mass of molecular gas is larger than the stellar mass within the inner $1' \times 1'$ Martinsson et al. (2013b).

The WHAN diagram of NGC 3982 (Fig. 2) confirms the signature of a strong AGN (sAGN) at the nucleus within the inner arcsec (82pc) in agreement with the Seyfert 2 classification (e.g. Ho et al. 1997; Quillen et al. 2001; Véron-Cetty & Veron 2006; Tripp et al. 2010). This region also presents a higher velocity dispersion ($\sigma \geq 130 \text{ km s}^{-1}$) than its surroundings ($\sigma \leq 80 \text{ km s}^{-1}$)— see Fig. 2,

which could suggest the presence of a mild unresolved nuclear outflow. In addition, strong AGN signatures are also observed at about 328 pc ($4''$) from the nucleus, at locations that surround star forming regions in the ring. We attribute this signature to an underlying young/intermediate age stellar population with strong $H\alpha$ absorption leading to an underestimate of the $H\alpha$ flux and thus to a large $[NII]/H\alpha$ line ratio. This could also explain the weak AGN signatures at the surrounding regions, where the $H\alpha$ fluxes are weak. Another possibility to explain this emission, could be the presence of post-AGB stars as already claimed to explain the LIER emission in large samples of galaxies (Belfiore et al. 2016). The star forming regions identified in the flux maps and already known (e.g. de Vaucouleurs et al. 1980; Comerón et al. 2010) are properly classified

as “Starburst” by the WHAN diagram, although some “noise” is observed.

Large scale IFU observations show that the stellar and gas velocity fields are consistent with regular rotation (e.g. Westfall et al. 2011; Martinsson et al. 2013a), while our small scale gas kinematics suggest the presence of deviations from pure rotation, as observed in Fig. 6. By comparing the fitted parameters from the rotation disk model (Table 2) with those found in the literature, we observe a large discrepancy among the values for the large scale disk and ours. The major axis of the galaxy is oriented along $\Psi_0 = 25.1^\circ$, as quoted in the Hyperleđa database (Paturel et al. 2003). Ciesla et al. (2014) used observations at $8\mu\text{m}$ and $500\mu\text{m}$ with the Herschel telescope and found that the major axis of the mid infrared emission is oriented along $\Psi_0 = 138^\circ$ which is 40 degrees smaller than the 173 ± 2 derived from our internal gas kinematics, while Martinsson et al. (2013a) present [O III] and stellar kinematics measured for an $1'$ FoV from PPAk integral field spectroscopy and found $\Psi_0 = 191.6^\circ \pm 0.5^\circ$, which is about 20° larger than ours. These discrepancies are probably due to the distinct FoV of the observations and the complex gas motions present within the inner few hundred parsecs of the galaxy. The systemic velocity of the galaxy obtained here is in good agreement with that of Martinsson et al. (2013a) and quoted in the Hyperleđa database.

5.2 NGC4501

NGC 4501 belongs to the Virgo cluster. High-resolution interferometer observations of the ^{12}CO ($J = 1 - 0$) emission in the central 5 kpc using the Nobeyama Millimeter Array show two molecular gas structures: (i) a nuclear concentration within the inner $5''$ with mass of $1.3 \times 10^8 M_\odot$, showing non-circular motions and (ii) large scale spiral arms, along which molecular gas streaming motions towards the center are observed (Onodera 2004). Multiple large scale spiral arms and two small scale arms are observed in the B-band (Elmegreen & Elmegreen 1987) and K-band (Elmegreen et al. 1999) images. WFPC2 F606W HST images reveal nuclear dust spirals (Carollo et al. 1998).

Mazzalay et al. (2013) used near-infrared integral field spectroscopy of the inner $3'' \times 3''$ of NGC 4501 obtained with the SINFONI instrument on the Very Large Telescope (VLT) to map the H_2 $2.12\mu\text{m}$ emission. They found that the H_2 flux distribution shows two components: an asymmetric nuclear component surrounded by two arcs, one to the northwest and the other to the southeast of the nucleus, that seem to be correlated with nuclear dust lanes seen in an WFPC2 F547M HST image and located inside edges of two peaks seen in CO image from Onodera (2004), indicating that the warm molecular gas traced by the H_2 line emission is closer to the nucleus than the cold molecular gas. In addition, Mazzalay et al. (2013) report that the spectra of NGC 4501 show no sign of ionized gas emission (e.g. Bry). The stellar kinematics of the inner $3'' \times 3''$ shows regular rotation with the line of nodes oriented along $PA = 140^\circ$ east of north, while the H_2 kinematics shows additional non-circular motions (Mazzalay et al. 2014). The authors analyze the H_2 kinematics based on a residual map, constructed by subtracting a rotating disk model from the observed velocity field. This map shows two main structures: one observed in blueshift to the northwest of the nucleus, co-spatial with a dust spiral arm, and another to the southwest of the nucleus seen in redshift. Mazzalay et al. (2014) interpret these structures as being due to outflows from the nucleus.

Recently, Repetto et al. (2016) used the same GMOS-IFU data of NGC 4501 used in this work (from Gemini archive) to study the

gas kinematics and stellar populations. However, their analysis is presented only for the inner $6'.4 \times 5'.4$ nuclear region. The velocity field and FWHM map for the [N II] $\lambda 6583$ emission line shown in Repetto et al. (2016) is consistent with ours, although their maps are much “noisier” than ours. Repetto et al. (2016) found that old stellar populations dominate the continuum emission from the inner region of the galaxy. They conclude that the gas kinematics is dominated by non-circular motions and reproduced by an exponential disk model, with a maximum expansion velocity of 25 km s^{-1} and major axis along $\Psi_0 \approx 137^\circ$. The authors argue also that the kinematics of the NaD $\lambda 5892$ is consistent with outflowing material from the center of NGC 4501 along two inner pseudo-spiral arms.

Our orientation for the line of nodes of the gas velocity field is also in good agreement with that quoted in the Hyperleđa database ($\Psi_0 = 138^\circ$) for the large scale disc, as well as with those obtained for the central region from stellar kinematics of the inner $3'' \times 3''$ ($\Psi_0 = 140^\circ$ – Mazzalay et al. 2014) and $\text{H}\alpha$ velocity field of the inner $6'.4 \times 5'.4$ ($\Psi_0 = 137^\circ$ – Repetto et al. 2016), while the systemic velocity is about 25 km s^{-1} smaller than that obtained from the optical measurements and quoted in Hyperleđa database.

NGC 4501 is cataloged as harboring a Seyfert 2 nucleus (Véron-Cetty & Veron 2006), while according to our WHAN diagram its nuclear emission corresponds to a “weak AGN”. X-ray emission from the nucleus of this galaxy gives a low luminosity of $L_{2-10\text{keV}} \approx 3.5 \times 10^{39} \text{ erg s}^{-1}$ (Liu 2011). A similar luminosity is also observed for the [O III] $\lambda 5007$ emission line, $L_{\text{OIII}} \approx 9.6 \times 10^{39} \text{ erg s}^{-1}$ (Brightman & Nandra 2008), while strong AGNs usually have larger [O III] luminosities. In addition, the nucleus of NGC 4501 falls at the region between Seyferts and LINERs in the [O III] $\lambda 5007/\text{H}\beta$ vs. [N II] $\lambda 6583/\text{H}\alpha$ diagnostic, as shown in (Brightman & Nandra 2008). Thus, our observations suggest that NGC 4501 nuclear activity is better classified as LINER, instead of Seyfert 2.

An intriguing feature is seen at $\sim 6''$ west of the nucleus, where the WHAN diagram shows AGN values (very close to the corner – in the WHAN diagram – that separates Starbursts, strong and weak AGNs). We attribute this apparent sAGN excitation as being due to the presence of a young stellar cluster, as indicated by a slightly enhancement in the $\text{H}\alpha$ flux map of Fig. A2, and possible shocks due to supernovae explosions, that would enhance the [N II]/ $\text{H}\alpha$ line ratio (e.g. Sutherland et al. 1993; Viegas & Contini 1994; Storchi-Bergmann et al. 2007). Assuming the $\text{H}\alpha$ emission is originated by gas photo-ionized by young stars, and using the photo-ionization models from Dors et al. (2008) and the observed $\text{H}\alpha$ equivalent width for position A, we estimate an age of $> 10 \text{ Myr}$, which is consistent with the presence of evolved stars.

5.3 NGC2787

Using long-slit spectra obtained with HST STIS at parsec-scale resolution, Sarzi et al. (2001) derived the mass of the SMBH as being about $10^8 M_\odot$, by modeling the gas kinematics. HST and ground based broad band images show a very complex morphology comprising a large inner disk, a nuclear bar oriented along $PA \sim -20^\circ$ and an off-plane dust disk in the central regions (e.g. Sarzi et al. 2001; Erwin & Sparke 2003a,b). Inside the bar, the inner disk is tilted relative to the orientation of the stellar distribution (Erwin & Sparke 2002), while the large scale H I distribution is also found to be misaligned relative to the optical emission, suggesting the presence of a dark halo (Shostak 1987). Chandra 0.5–1.5 keV observations show unresolved nuclear emission consistent with a stellar origin, with only a small contribution from hot gas (Li et al. 2011).

So far, there are no studies available about the gas and stellar kinematics of the central region of NGC 2787.

NGC 2787 shows a WHAN diagram (Fig. 4) with wAGN signature observed at the nucleus and RG signatures elsewhere, confirming that its nuclear activity is of the LINER type (Véron-Cetty & Veron 2006), with a weak broad $H\alpha$ component observed at the nuclear spectrum (Fig. 1), already previously detected (Ho et al. 1997).

The systemic velocity for NGC 2787 derived in Sec. 4 is in reasonable agreement with that presented at Hyperleda database ($v_s = 606 \pm 40 \text{ km s}^{-1}$), while the orientation of the line of nodes that we have obtained is 37° smaller than the PA of the major axis of the large scale disk listed in Hyperleda. On the other hand, it is known that NGC 2787 present a complex structure in the central region (e.g. Erwin & Sparke 2003a,b) and thus a misalignment between the large and small scale disk can be expected. Indeed, the PA of the line of nodes we have derived for the circumnuclear gas kinematics of 100° is consistent with the orientation of the nuclear bar in HST images (Erwin & Sparke 2003b).

Another feature observed in the gas velocity field is an increase in the velocity dispersion at the nucleus extending to $\approx 2''$ (126 pc) to the south of the nucleus, which could indicate a mild AGN outflow.

5.4 NGC 4450

NGC 4450 is an anemic spiral galaxy in the Virgo cluster. Its nuclear spectrum shows a weak broad double-peaked $H\alpha$ profile, interpreted as the signature of the outer parts of a relativistic accretion disk (Ho et al. 1997). Fabry-Perot observations at a seeing of $\sim 1.5''$ and a field of $1.8'$ reveal a patchy $H\alpha$ distribution and a perturbed velocity field with the orientation of the line of nodes along $PA = 351^\circ \pm 9^\circ$ east of north and with a steep velocity gradient of 200 km s^{-1} around the nucleus (Chemin et al. 2006). Similar distribution is observed in H I emission (Cayatte et al. 1990). Interferometric observations show only weak CO emission and a total mass of cold gas of $\sim 10^9 M_\odot$ is observed for the whole galaxy (Helfer et al. 2003). The nuclear region of NGC 4450 shows two long dusty spirals in the main disk along with some flocculent structures, but with no star formation associated to the dusty spirals (Elmegreen et al. 2002).

Cortés, Kenney & Hardy (2015) present optical IFU observations of the inner $20'' \times 40''$ of NGC 4450. They found that the stellar velocity field is dominated by rotation, but very perturbed, with the orientation of the line of nodes changing from 175° at the center to 160° at $15\text{--}25''$ of the nucleus. The [O III] velocity field is misaligned relative to the stellar kinematics, with the orientation of the line of nodes along $PA \sim 190^\circ$ east of north. Cortés, Kenney & Hardy (2015) interpret this misalignment as being due to non-circular motions or due to emission of gas located in a tilted gas disk relative to the stellar disk, produced by an accretion event or minor merger.

The orientation of the line of nodes derived in Sec. 4 ($\Psi_0 = 192^\circ$) is in good agreement with that of the large scale disk (Dicaire et al. 2008), and consistent with the orientation of the line of nodes observed for the [O III] emission at the inner $20''$ (Cortés, Kenney & Hardy 2015). A knot of residual blueshift (after the subtraction of the rotation model) at $\approx 1''$ (81 pc) to the east of the nucleus (the near side of the galaxy) and residual redshift at a similar distance to the west (the far side of the galaxy) possibly indicate the presence of a nuclear outflow in the east-west direction (direction of the largest extent of the [NII] flux map). However it should

be noticed that the size of the structures seen in blueshifts and redshifts in the residual maps are comparable to the spatial resolution of our data. Another feature of the gas kinematics that our measurements revealed is an increase in the [NII] velocity dispersion at the nucleus, which could be due to a previous plasma ejection related to the compact nuclear outflow. Alternatively, the larger velocity dispersion at the nucleus could also be due to unresolved rotation.

Our WHAN diagram for NGC 4450 shows strong AGN features in the inner $0''.5$, surrounded by a ring of weak AGN signature. NGC 4450 was previously cataloged as harboring a LINER nucleus (Véron-Cetty & Veron 2006; Kewley et al. 2006), but it presents stronger X-ray emission than NGC 4501, originally classified as Seyfert and with a WHAN diagram indicating that Seyfert is better classification for its nuclear emission. Liu (2011) presents a 0.3–8 keV flux of $1.19 \times 10^{-12} \text{ erg s}^{-1}$, which corresponds to a luminosity of $L_{0.3\text{--}8 \text{ KeV}} \approx 3.6 \times 10^{40} \text{ erg s}^{-1}$, that is one order of magnitude larger than the values observed for NGC 2787 and NGC 4501. On the other hand, NGC 4450 shows a low [O III] $\lambda 5007$ luminosity ($L_{\text{OIII}} \approx 6 \times 10^{38} \text{ erg s}^{-1}$, Balmaverde & Capetti 2013), smaller than commonly observed in sAGNs.

5.5 Residual gas velocity maps vs. nuclear spirals

The velocity residual maps (obtained as the difference between the observed velocity fields and the rotation model) for NGC 4501 and NGC 4450 show that many of the kinematic structures of these maps are spatially correlated with the dust features seen in the structure map. The residual maps are shown in the central panels of Figs. 6–9. The residual map for NGC 3982 shows some structures revealing the presence of non-circular motions, although only a few of these structures are correlated with dust features. For NGC 2787 (Fig. 8) the velocity residuals are small at all locations and no systematic structures are seen in the residual map, indicating that the adopted model is a good representation of the observed velocity field, which is dominated by the rotating disk component.

In order to better analyze the structures in the velocity residual maps, we assume that the spiral arms observed in the large scale images are trailing to determine the near and far side of the disk, identified in the central panels of Figs. 6–9 that show the rotation model for each galaxy. We also show in these figures the structure maps at the same scale as the kinematic maps in order to verify possible correlations between dust and kinematic structures in the residual maps. This is motivated by previous results from our group in which we have found an association between gas inflows and nuclear spiral arms (e.g. Fathi et al. 2006; Storchi-Bergmann et al. 2007; Riffel et al. 2008; Riffel, Storchi-Bergmann & Winge 2013; Schnorr-Müller et al. 2014a).

The residual map for NGC 3982 shows that the highest blueshifts of up to $\sim -50 \text{ km s}^{-1}$ are observed to the N-NE of the nucleus in the far side of the galaxy, in a region where the structure map shows a strong dust spiral arm. In addition, some redshifts are also observed associated to the inner part of the same spiral arm, but in the near side of the galaxy. A possible interpretation to this residuals is that they represent inflows of gas towards the nucleus. However, this interpretation should be taken with caution, as residuals of the order of $20\text{--}40 \text{ km s}^{-1}$ are observed also at other locations of the galaxy. We can thus only state with certainty that the velocity residuals are correlated with the dust structures seen in the nuclear region.

A correlation between the velocity residuals and the dust structures is also observed for NGC 4501, as can be seen by comparing the central-right and right panels of Fig. 7. Besides these

correlations, a “redshifted blob” is observed at 1–3'' SW of the nucleus. A similar structure was observed by Mazzalay et al. (2014) in a residual map for the H₂ kinematics, and interpreted as due to an outflow, together with an arc-shaped blueshifted outflow in the near side of the galaxy. These kinematic structures are also supported by Repetto et al. (2016). The outflow interpretation for the redshifted blob is supported, in our observations, by an increase in the gas velocity dispersion at the location of the blob, as seen in Fig. 3 and Fig. A2. In addition, some blueshifts to the west (in the far side of the galaxy) and redshifts to the east (in the near side of the galaxy) could be attributed to inflows towards the nucleus, but there are also similar residuals at other locations and again we can only state that these residuals are associated with the dust structures.

Finally, for NGC4450, the residual map shows blueshifts of up to -100 km s^{-1} , as well as similarly high redshifts. A disturbed kinematics for the gas in the central region of this galaxy has already been claimed by Cortés, Kenney & Hardy (2015), who showed that the [O III] kinematics was misaligned relative to the stellar kinematics. Besides the usual correlation between the residuals and the dust structures, blueshifts of up to 150 km s^{-1} at 0'.5 NE of the nucleus and some redshifts observed at similar distance to the SW could be interpreted as due to a bi-conical outflow, although this is only a speculation, as other similar residuals are observed at other locations. The presence of a nuclear outflow is also supported by the increased velocity dispersion observed within the inner 1'' (Fig. 5).

In summary, the gas kinematics, although dominated by rotation, shows deviations correlated with dust structures. Such structures usually trace shocks in the gas and we speculate that we are probing these shocks that may lead to loss of angular momentum allowing for the gas to move inwards to feed the AGN at the nuclei of the galaxies.

6 CONCLUSIONS

We have mapped the ionized gas kinematics and flux distributions in the central kiloparsec of NGC 3982, NGC 4501, NGC 2787 and NGC 4450 using GMOS IFS at a velocity resolution of $\sim 120 \text{ km s}^{-1}$ and spatial resolution in the range 50–70 pc. The four galaxies show extended emission for H α , [N II] and [S II] emission lines, while [O I] extended emission was observed only for NGC 3982, to up to 2'' from the nucleus. The main conclusions of this work are:

- The velocity field of all galaxies are dominated by rotation and reproduced by a disk model, under the assumption that the gas rotates at the plane of the galaxy at circular orbits.
- Besides the rotating disk component, the gas in NGC 3982, NGC 4501 and NGC 4450 show non-circular motions, evidenced in the residual (observed velocity – rotation mode) velocity maps. At least for the latter two, these residuals are associated with dust features revealed in the structure maps.
- The velocity residual map for NGC4501 reveals also a redshifted blob in the far side of the galaxy at 1–2'' SW of the nucleus that can be interpreted as due to a nuclear outflow. Possible outflows are also observed in NGC4450 as blueshifts and redshifts within the inner 1'' to the northeast and southwest, respectively.
- NGC 2787 shows a very regular rotation with the orientation of the line of nodes misaligned by $\sim 40^\circ$ relative to the large scale disk. This galaxy is known to show a complex morphology at the central region and the PA of the line of nodes is consistent with the orientation of a nuclear bar.

- The H α equivalent width ($W_{H\alpha}$) vs. [N II]/H α (WHAN) diagrams show a wide range of values, with the nuclear emission of NGC 3982 and NGC 4450 showing a Seyfert signature, while for NGC2787 and NGC4101 a LINER signature is obtained.

- NGC 3982 shows a clear circumnuclear star-formation ring surrounding the nucleus at 4–6'', as seen in the flux maps and in the WHAN diagram.

- A star forming region was detected at 6'' west of the nucleus of NGC 4501. The WHAN diagram shows values typical of Seyfert galaxies for this region and we interpret it as being originated by emission enhanced due to shocks from supernovae explosions.

- The excitation maps show that the AGN emission is very compact for all galaxies, being unresolved for NGC 4501, NGC 4450 and NGC 4450.

ACKNOWLEDGEMENTS

This work is based on observations obtained at the Gemini Observatory, which is operated by the Association of Universities for Research in Astronomy, Inc., under a cooperative agreement with the NSF on behalf of the Gemini partnership: the National Science Foundation (United States), the Science and Technology Facilities Council (United Kingdom), the National Research Council (Canada), CONICYT (Chile), the Australian Research Council (Australia), Ministério da Ciência e Tecnologia (Brazil) and south-east CYT (Argentina). C.B thanks to CNPq for financial support. R.A.R. acknowledges support from FAPERGS (project N0. 2366-2551/14-0) and CNPq (project N0. 470090/2013-8 and 302683/2013-5).

REFERENCES

- Allen, M., G., Dopita, M., A., Tsvetanov, Z. 1998, AJ, 493, 571.
- Allington-Smith, J., Graham, M., Content, R., Dodsworth, G., Davies, R., Miller, B. W., Jorgensen, I., Hook, I., Crampton, D., Murowinski, R., 2002, PASP, 114, 892.
- Baillard, A., et al. 2011, A&A, 532, A74.
- Balmaverde, B., Capetti, A., 2013, A&A, 549, 114.
- Baldwin, J. A., Phillips, M. M., Terlevich, R., 1981, PASP, 93, 5.
- Belfiore, F., et al. 2016, MNRAS, 461, 3111.
- Bertola, F., Bettoni, D., Danziger, J., 1991, ApJ, 373, 369.
- Brightman, M., Nandra, K., 2008, MNRAS, 390, 1241.
- Bruzual, G. & Charlot, S. 2003, MNRAS, 344, 1000
- Caldwell, N., Rose, J. A., & Dendy, K. 1999, AJ, 117, 140
- Capelo, P. R. & Dotti, M., 2017, MNRAS, 465, 2643.
- Cappellari, M., Emsellem, E. 2004, PASP, 116, 138.
- Cayatte, V., van Gorkom, J. H., Balkowski, C., Kotanyi, C., 1990, AJ, 100, 604.
- Carollo C. M., Stiavelli M., Mack J., 1998, AJ, 116, 68
- Cid Fernandes, R., Stasińska G., Schlickmann M. S., Mateus A., Vale Asari N., Schoenell W., Sodré L., 2010, MNRAS, 403, 1687
- Cid Fernandes, R., Stasińska G., Mateus A., Vale Asari, 2011, MNRAS, 413, 1036
- Ciesla, L., Boquien, M., Boselli, A., Buat, V., Cortese, L., Bendo, G. J., Heinis, S., Galametz, M., Eales, S., Smith, M. W. L., Baes, M., Bianchi, S., de Looze, I., di Serego Alighieri, S., Galliano, F., et al. 2014, A&A, 565, 128
- Chemin, L., Balkowski, C., Cayatte, V., Carignan, C., Amram, P., Garrido, O., Hernandez, O., Marcelin, M., Adami, C., Boselli, A., Boulesteix, J., 2006, MNRAS, 812, 857.

- Colina L., Piqueras-Lopez J., Arribas S., R. Riffel, Rodriguez-Ardila, Pastoriza, M. G., Storchi-Bergmann T., Alonso-Herrero & Sales D., 2015, *A&A*, 578, 48.
- Comerón, S., Knapen, J. H., Beckman, J. E., Laurikainen, E., Salo, H., Martinez - Valpuesta, I., Buta, R. J. 2010 *MNRAS*, 402, 2462
- Cortés, J. R., Kenney, J. D. P., Hardy, E., 2015, *ApJ&SS*, 216, 9
- Couto, Guilherme S., Storchi-Bergmann T., Axon, David J., Robinson, A., Kharb, P., and Riffel, R. A., 2013, *MNRAS*, 435, 2982
- de Vaucouleurs, G., Buta, R. J., *AJ*, 85, 637
- de Vaucouleurs, G., de Vaucouleurs, A., Corwin, H. G. Jr, Buta, R. J., Paturel, G., Fouque, P., 1991, *Third Reference Catalogue of Bright Galaxies*, Vols 1–3, Springer-Verlag, Berlin
- Dicaire, I., Carignan, C., Amram, P., Hernandez, O., Chemin, L., Daigle, O., de Denus-Baillargeon, M.-M., Balkowski, C., Boselli, A., Fathi, K., Kennicutt, R. C., 2008 *MNRAS*, 385, 553.
- Dors, O. L., Jr., Storchi-Bergmann, T., Riffel, R. A., Schimdt, Alex. A., 2008, *A&A*, 428, 59.
- Elmegreen D. M., Elmegreen B. G., 1987, *ApJ*, 314, 3
- Elmegreen D. M., Chromey F. R., Bissell B. A., Corrado K., 1999, *AJ*, 118, 2618
- Emsellem, E., Goudfrooij, P., & Ferruit, P. 2003, *MNRAS*, 345, 1297
- Emsellem, E., Fathi, K., Wozniak, H., Ferruit, P., Mundell, C. G., Schinnerer, E. 2006, *MNRAS*, 365, 367
- Emsellem, E., Renaud, F., Bournaud, F., Elmegreen, B., Combes, F., Gabor, J. M., 2015, *MNRAS*, 446, 2468
- Englmaier, P., & Shlosman, I. 2004, *ApJ*, 617, L115
- Elmegreen, D. M. and Elmegreen, B. G. and Eberwein, K. S., 2002 *ApJ*, 564, 243
- Erwin, P., Sparke L. S., 1999, *ASP Conf. Ser. Vol. 182. Galaxy Dynamics - A Rutgers Symposium*. Astron. Soc. Pac., San Francisco, p. 243
- Erwin, P., Sparke L. S., 2002, *AJ*, 124, 65
- Erwin, P., Sparke L. S., 2003, *ApJS*, 146, 299
- Erwin, P., Beltrán, J. C. V., Graham, A. W. and Beckman, J. E., 2003, *ApJ*, 597, 947
- Fathi, K., Storchi-Bergmann, T., Riffel, R. A., Winge, C., Axon, D. J., Robinson, A., Capetti, A., & Marconi, A., 2006, *ApJ*, 641, L25.
- Feltre, A., Charlot, S., Gutkin, J., 2016, 456, 3354.
- Gonzalez-Martin, O., Masegosa, J., Marquez, I., Guainazzi, M., Jimenez-Bailon, E. 2009, *A&A*, 506, 1107.
- Helfer, T. T., Thornley, M. D., Regan, M. W., Wong, T., Sheth, K., Vogel, S. N., Blitz, L., Bock, D. C.-J., 2003, *ApJS*, 145, 259.
- Ho, L. C., Filippenko, A. V., Sargent, W. L. 1997, *ApJ&SS*, 112, 315.
- Ho, L. C. 1999, *ApJ*, 516, 672.
- Ho, L., Rudnick, G., Rix, H-W, Shields, J. C., McIntosh, D. H., Filippenko, A. V., Sargent, W. L. W., Eracleous, M., 2000, *ApJ*, 541, 1.
- Ho, L. C., Ulvestad, J.S., 2001, *ApJS*, 133, 77.
- Hook, I., Jorgensen, I., Allington-Smith, J. R., Davies, R. L., Metcalfe, N., Murowinski, R. G., Crampton, D., 2004, *PASP*, 116, 425
- Kauffmann, G., Heckman, T. M., Tremonti, C., Brinchmann, J., Charlot, S., White, S. D. M., Ridgway, S. E., Brinkmann, J., Fukugita, M., Hall, P. B., Ivezi, ., Richards, G. T., Schneider, D. P., 2003, *MNRAS*, 346, 1055
- Kewley, L. J., Heisler, C. A., Dopita, M. A., 2001, *ApJS*, 132, 37.
- Kewley, L. J., Groves, B., Kauffmann, G., Heckman, T., 2006, *MNRAS*, 372, 961
- Knapen, J. H., Prez-Ramrez, D., Laine, S., 2002, *MNRAS* 337, 808.
- Knapen, J. H. 2005, *ApJ&SS* 295, 85.
- Koopmann, R. A., Kenney, J. D. P., Young, J., 2001, *ApJS* 135, 125.
- Kraemer, S. B., Schmitt, H. R., Crenshaw, D. M., Melndez, M., Turner, T. J., Guainazzi M., Mushotzky, R. F., 2011, *ApJ* 727, 130
- Laine S., van der Marel R. P., Rossa J., Hibbard J. E., Mihos J. C., Böker T., Zabludoff A. I., 2003, *AJ*, 79, 745
- Lena, D. and Robinson, A., Storchi-Bergmann, T., Schnorr-Müller, A., Seelig, T., Riffel, R. A., Nagar, N. M., Couto, G. S. and Shadler, L., 2015, *ApJ*, 806, 84
- Lena, D. and Robinson, A., Storchi-Bergmann, T., Couto, G. S., Schnorr-Müller, A., Riffel, R. A., 2016, *MNRAS*, 459, 4485.
- Li, J-T., Wang, Q. D., Li, Z., Chen, Y., 2011, *ApJ*, 737, 41.
- Li, Z. Shen, J., Kim, W-T., 2015, *ApJ*, 806, 150.
- Liu, J., 2011, *ApJS*, 192, 10.
- Maciejewski, W., Teuben, P. J., Sparke, L. S., & Stone, J. M. 2002, *MNRAS*, 329, 502.
- Malkan, M. A., Gorjian, V. & Tam, R., 1998, *ApJS*, 117,25.
- Markwardt C. B., 2009, in Bohlender D. A., Durand D., Dowler P., eds, *ASP Conf. Ser. Vol. 411, Astronomical Data Analysis Software and Systems XVIII*. Astron. Soc. Pac., San Francisco, p. 251
- Martinsson, T. P. K., Verheijen, M. A. W., Westfall, K. B., Bershadly, M. A., Schechtman - Root, A., Andersen, D. R., Swaters, R. A., 2013, *A&A*, 557, A130
- Martinsson, T. P. K., Verheijen, M. A. W., Westfall, K. B., Bershadly, M. A., Schechtman - Root, A., Andersen, D. R., Swaters, R. A., 2013, *A&A*, 557, A131
- Mazzalay, X. et al., 2013, *MNRAS*, 428, 2389.
- Mazzalay, X. et al., 2014, *MNRAS*, 438, 2036.
- Melndez, M., Kraemer, S. B., Schmitt, H. R., Crenshaw, D. M., Deo, R., P., Mushotzky, R. F., Bruhweiler, F. C., 2008, *ApJ*, 689, 95.
- Munoz Marin, V. M. et al., 2007, *AJ*, 134, 648.
- Onodera, S. and Koda, J. and Sofue, Y. and Kohno, K., 2004, *PASJ*, 56, 439
- Osterbrock D. E., 1989, *Astrophysics of Gaseous Nebulae and Active Galactic Nuclei*. University Science Books, Mill Valley, CA.
- Paturel, G., Petit, C., Prugniel, Ph., Theureau, G., Rousseau, J., Brouty, M., Dubois, P. & Cambrésy, L., 2003, *A&A*, 412, 45.
- Pérez-Ramírez, D., Knapen, J. H., Peletier, R. F., Laine, S., Doyon, R., Nadeau, D., 2000, *MNRAS*, 317, 234.
- Pogge R. W., Martini P., 2002, *ApJ*, 569, 624
- Quillen, A. C., Alonso-Herrero, A., Lee, A., Shaked, S., Rieke, M. J., Rieke, G. H. 2001, *ApJ*, 547, 129
- Regan, M. W. et al., 1999, *ApJ*, 117, 2676.
- Rembold, S. et al., 2016, *MNRAS*, submitted.
- Repetto, P., Fandez-Abans, M., Freitas-Lemes, P., Rodrigues, I., de Oliveira-Abans, M., 2016, *MNRAS*, 464, 293
- Reunanen, J., Kotilainen, J. K., & Prieto, M. A., 2002, *MNRAS*, 331, 154.
- Riffel, Rogemar A., Rodriguez-Ardila A., Pastoriza M. G., 2006b, *A&A*, 457, 61.
- Riffel, Rogemar A., Storchi-Bergmann, T., Winge, C., McGregor, P. J., Beck, T., Schmitt, H. 2008, *MNRAS*, 385, 1129.
- Riffel R. A., 2010, *Ap&SS*, 327, 239.
- Riffel, Rogemar A., Storchi-Bergmann, T. & Nagar, N. M., 2010a, *MNRAS*, 404, 166.

- Riffel, Rogemar A. & Storchi-Bergmann, T., Riffel, R., & Pastoriza, M. G., 2010, *ApJ*, 713, 469.
- Riffel, Rogemar A. & Storchi-Bergmann, T., 2011, *MNRAS*, 411, 469.
- Riffel, R. A., Storchi-Bergmann, T., Winge, C., 2013, 430, 2249.
- Riffel, Rogemar A. & Storchi-Bergmann, T. & Riffel, R., 2015, *MNRAS*, 451, 3587.
- Riffel, Rogemar A., Storchi-Bergmann, T., Riffel, R., Dahmer-Hahn, L. G., Diniz, M. R., Schönell, A. J., Dametto, N. Z., 2017, *MNRAS*, submitted.
- Riffel, R., Riffel, Rogemar A., Ferrari, F., & Storchi-Bergmann, T., 2011, *MNRAS*, 416, 493.
- Rodríguez-Ardila, A., Pastoriza, M. G., Viegas, S., Sigut, T. A. A., & Pradhan, A. K., 2004, *A&A*, 425, 457.
- Sakamoto K., Okumura S. K., Ishizuki S., Scoville N. Z., 1999, *ApJ*, 525, 691
- Sanchez, S. et. al. 2015, *A&A*, 574, A47.
- Sarzi, M., et. al. 2010, *MNRAS*, 402, 2187.
- Sarzi, M., Sarzi, M., Rix, H.-W., Shields, J. C., Rudnick, G., Ho, L. C., McIntosh, D. H., Filippenko, A. V., & Sargent, W. L. W. 2001, *ApJ*, 550, 65
- Schnorr Müller A., Storchi-Bergmann T., Riffel R. A., Ferrari F., Steiner J. E., Axon D. J., Robinson A., 2011, *MNRAS*, 413, 149
- Schnorr Müller A., Storchi-Bergmann T., Nagar, N. M., & Ferrari, F. 2014a, *MNRAS*, 438, 3322
- Schnorr Müller A., Storchi-Bergmann T., Nagar, N. M., & Robinson, A., Lena, D., Riffel, R. A., Couto, G. S., 2014b, *MNRAS*, 437, 1708.
- Shlosman, I., Begelman, M. C., & Frank, J. 1990, *Nature*, 345, 679
- Shostak, G. S. 1987, *A&A*, 175, 4.
- Simões Lopes, R. D., Storchi-Bergmann, T., de Fátima Saraiva, M. and Martini, P., 2007, *ApJ*, 655, 718
- Storchi-Bergmann, T., Dors Jr., O., Riffel, R. A., Fathi, K., Axon, D. J., & Robinson, A., 2007, *ApJ*, x, x
- Sutherland, R. S., Bicknell, G. V., Dopita, M. A., 1993, *ApJ*, 414, 510.
- Trippe, M. L., Crenshaw, D. M., Deo, R. P., Dietrich, M. Kraemer, S. B., Rafter, S. E., Turner, T. J., *ApJ*, 725, 1749
- van der Kruit, P. C., & Allen, R. J. 1978, *ARA&A*, 16, 103
- Véron-Cetty, M. P., & Véron, P., 2006, *A&A*, 455, 773.
- Viegas, S., Contini, M., 1994, *ApJ*, 428, 113.
- Young, J. S., Allen, L., Kenney, J. D. P., Lesser, A., Rownd, B., 1996, *AJ*, 112, 1903.
- Westfall, K. B., Bershad, M. A., Verheijen, M. A. W., 2011, *ApJS*, 193, 21.

APPENDIX A: FLUX DISTRIBUTIONS AND KINEMATICS

Figures A1 to A4 show maps for the flux distributions, centroid velocity and velocity dispersion of the $H\alpha$ [S II] $\lambda 6730$ and [O I] $\lambda 6300$ emission lines for NGC 3982, NGC 4501, NGC 2787 and NGC 4450.

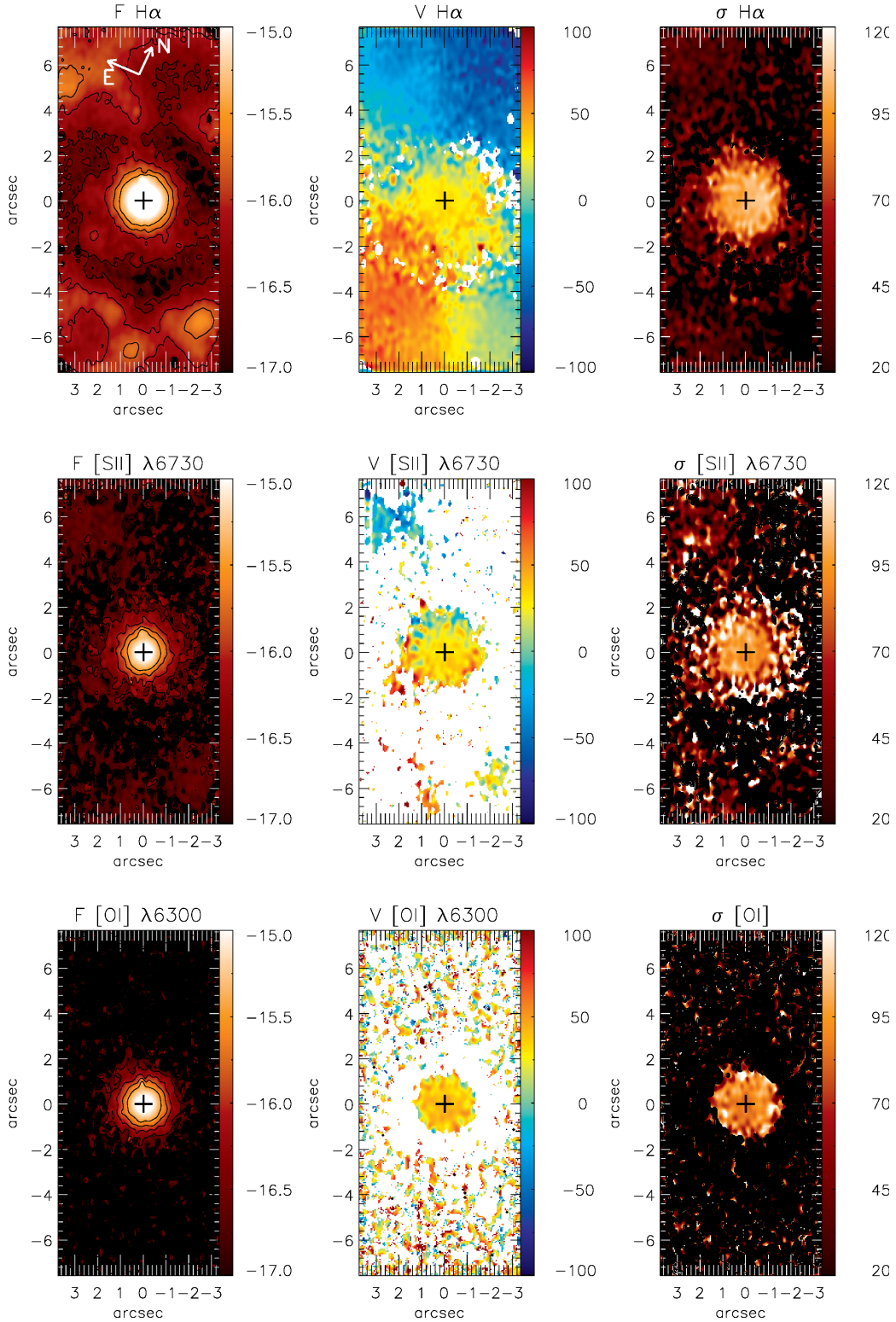


Figure A1. Flux distributions for $H\alpha$, $[S II] \lambda 6730$ and $[O I] \lambda 6300$ emission lines. The color bars show the flux scale in units of $10^{-17} \text{ erg s}^{-1} \text{ cm}^{-2}$ and the central cross marks the position of the nucleus. Black regions mark masked regions and corresponds to locations where no good fits of the line profiles could be obtained. Centroid velocity fields for the $H\alpha$, $[S II]$ and $[O I]$ emitting gas. The central crosses mark the position of the nucleus and color bars show the observed velocities in units of km s^{-1} relative to the systemic velocity of the galaxy. White regions correspond to locations where the lines were not detected or no good fits were possible. Velocity dispersion (σ) maps for $H\alpha$, $[S II]$ and $[O I]$ emission lines for NGC 3982. The central crosses mark the position of the nucleus and the color bars show the σ values in km s^{-1} . Black regions correspond to locations where the lines were not detected or no good fits were possible.

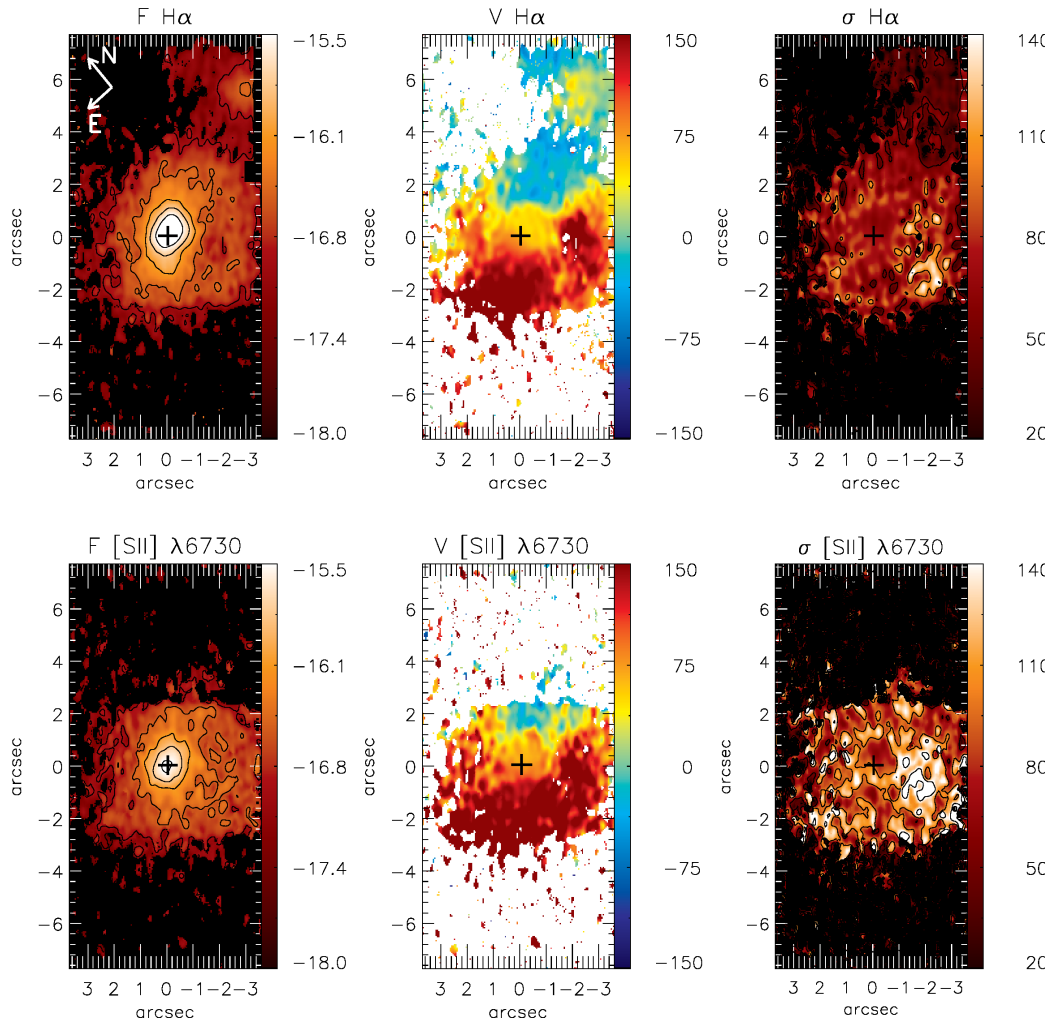


Figure A2. Same as Fig. A1 for NGC 4501

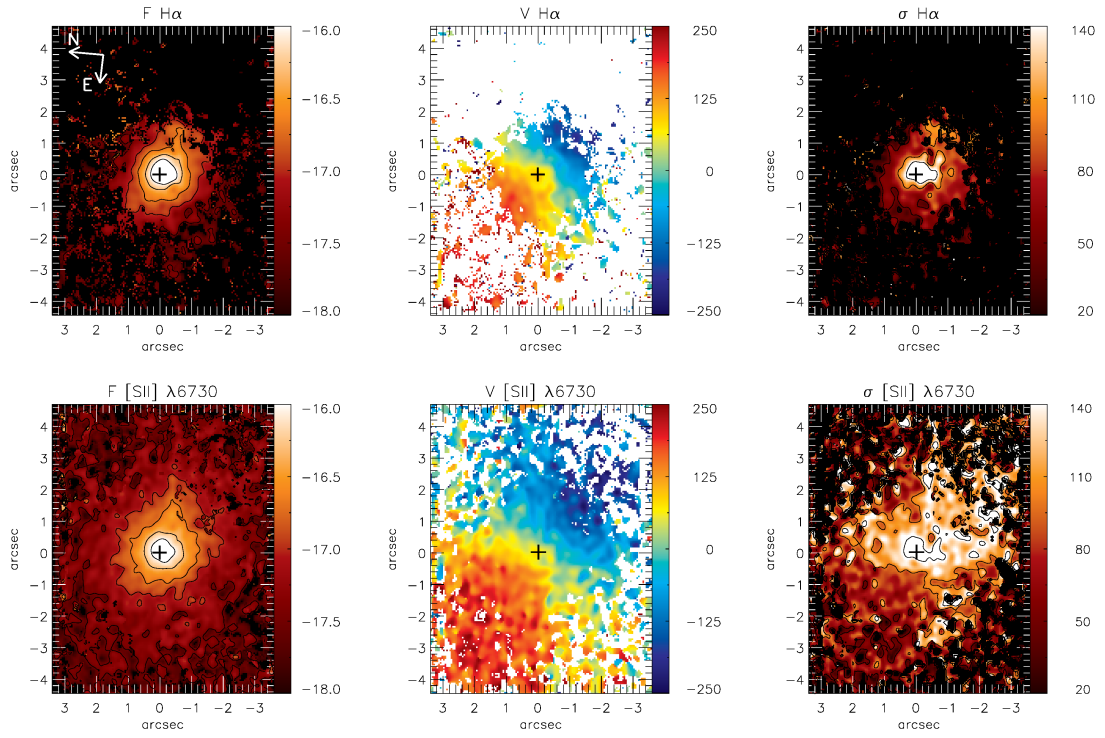


Figure A3. Same as Fig. A1 for NGC 2787

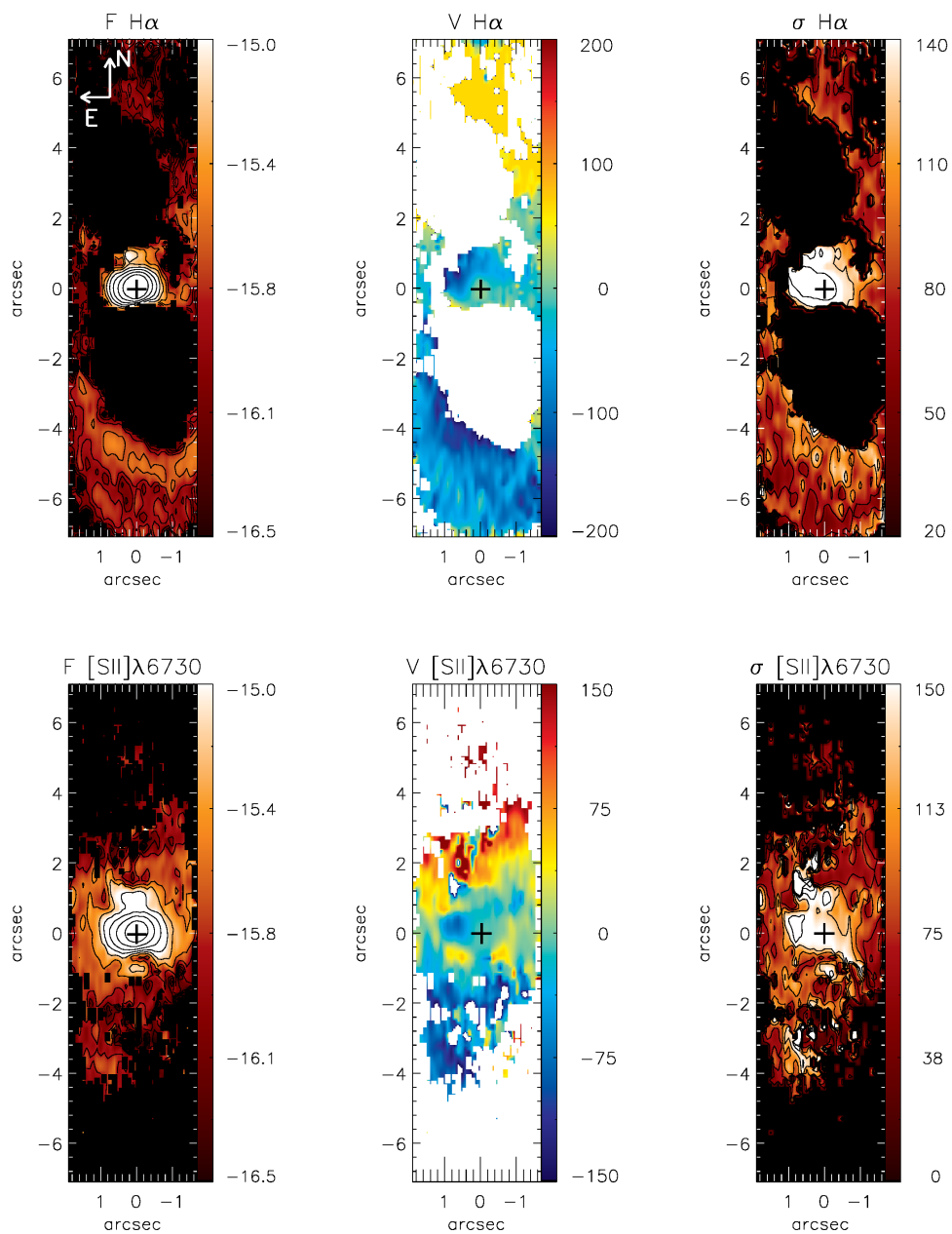


Figure A4. Same as Fig. A1 for NGC 4450